Materials Horizons

ROYAL SOCIETY OF CHEMISTRY

COMMUNICATION

View Article Online
View Journal | View Issue

Check for updates

Cite this: *Mater. Horiz.*, 2026, 13, 454

Received 23rd July 2025,
Accepted 29th September 2025

DOI: 10.1039/d5mh01415h

rsc.li/materials-horizons

A bipolar response deep ultraviolet photodetector for encryption and anti-interference communication based on an a-Sb_2O_5/a-Ga_2O_3 heterojunction

Cheng Wu,[ab] Peiwen Lv, *[abc] Zhaojie Zhu,[ac] Yizhi Huang,[ac] Chaoyang Tu,[ac]
Chenlong Chen,[ac] G. Lakshminarayana[d] and Yan Wang *[ac]

The integration of positive photoconductivity (PPC) and negative photoconductivity (NPC) significantly enhances the functionality of photodetectors. Sb(V)-based oxides are gaining prominence in advanced applications due to their notably deep band edges and favorable band alignment characteristics that benefit the photoelectric interface. The deep ultraviolet photodetector based on the a-Sb_2O_5/a-Ga_2O_3 heterostructure demonstrates wavelength–voltage synergistic bipolar photocurrent switching, attributed to the carrier trapping mechanism at the interface states. This detector exhibits an NPC responsivity of 0.71 mA W^{-1} (at 0 V, 287 nm) and a PPC responsivity of 1.05 mA W^{-1} (at 1 V, 303 nm). Furthermore, it shows a bidirectional photocurrent with short-wavelength NPC and long-wavelength PPC at a transition voltage of 0.5 V. Based on the bidirectional photoresponse, the detector not only enhances the confidentiality of real-time communication through bipolar coding technology but also reduces the detector's bit error rate *via* redundant error correction through bipolar channels. The wavelength–voltage synergistically controlled bipolar response of the a-Sb_2O_5/a-Ga_2O_3 heterojunction exhibits significant potential for developing novel optical communication devices suited for specialized environments.

New concepts

The combination of positive photoconductivity (PPC) and negative photoconductivity (NPC) has broad application prospects in photodetection, serving as an important foundation for realizing multifunctional integrated optoelectronic devices. However, most devices exhibiting bipolar responses are limited to a certain group of materials with a particular structure, and the switching between NPC and PPC relies entirely on wavelength control, making synchronous temporal modulation unattainable and thereby restricting their use in fields such as radiation detection and deep-ultraviolet detection. Therefore, a novel bipolar response deep ultraviolet photodetector based on an a-Sb_2O_5/a-Ga_2O_3 heterojunction has been constructed. Compared with conventional photodetectors, it exhibits wavelength–voltage synergistically controlled bipolar switching between NPC and PPC within the deep-ultraviolet range. This breakthrough finding not only enhances the security of real-time communications through bipolar encoding but also reduces the bit error rate of the detector by redundant error correction in bipolar channels. Therefore, the present work exhibits significant potential for developing novel optical communication devices suited for specialized environments.

1. Introduction

As a core component of modern optoelectronic technology,[1] photodetectors are widely employed in optical communication,[2–4] multispectral imaging,[5,6] and environmental monitoring.[7,8] Traditional photodetectors primarily rely on the positive photoconductivity (PPC) of semiconductor materials, which exhibit increased conductivity under illumination.[9–11] However, this type of detector cannot satisfy the demands for new functional applications driven by the rapid advancement of information technology,[12] and attempts to develop multifunctional detectors only by improved integration will face challenges such as high-power consumption, complex design, and information crosstalk.

In recent years, with the discovery of negative photoconductivity (NPC) in 2D materials, the function of PPC devices can be expanded by combining an NPC response,[13] which can not only reduce the power consumption of the device,[14] but also solve the problem of single function and lack of multi-mode adjustment of conventional photodetectors.[15–18] Baek *et al.* observed negative photoconductivity in Si nanowire field effect transistors (FETs) with different doping concentrations and revealed that the light-dependent switching between NPC and PPC is determined by the competition between the interfacial trapping and the mobile carrier recombination.[19] Xue *et al.* reported an organic phototransistor (OPT) with a bidirectional

---

[a] *State Key Laboratory of Functional Crystals and Devices, Fujian Institute of Research on the Structure of Matter, Chinese Academy of Sciences, Fuzhou City, Fujian Province, 350002, P. R. China. E-mail: pwlv@fjirsm.ac.cn, wy@fjirsm.ac.cn*
[b] *University of Chinese Academy of Sciences, Bei Jing City, 100039, P. R. China*
[c] *Fujian Science & Technology Innovation Laboratory for Optoelectronic Information of China (Mindu Innovation Laboratory), Fuzhou, Fujian, 350108, P. R. China*
[d] *Future Technology School, Shenzhen Technology University, Shenzhen, 518118, P. R. China*

photoresponse constructed with $F_{16}CuPc$.[20] The different light absorption of each layer of the heterojunction makes it have a wavelength-selective NPC response, and the high-contrast imaging of the detector is realized by using the photocurrent decreasing characteristics of NPC and the photocurrent increasing characteristics of PPC. Xu *et al.* developed an AMI/HDB_3 ternary coded underwater encrypted communication system by using the Cu_2O modified α-Ga_2O_3 nanorod array that can generate a bipolar photocurrent under dual-band ultraviolet light irradiation.[21] By using the superposition characteristics of the bipolar photocurrent, the concealment of information transmission is improved. Through the combination of ZnO nanowires and Sb_2Se_3 films, Ouyang *et al.* realized a wavelength-controlled bipolar response photodetector and successfully applied it to the color shift keying (CSK) system.[22] Its working efficiency is equivalent to two traditional receivers without any filters. Tang *et al.* demonstrated the ultra-low power switching between the light intensity-dependent NPC and PPC in the Gr/WSe_2 van der Waals heterojunction and successfully realized the simulation of low-power optoelectronic synapses by adjusting the optical pulse parameters, which promoted the development of neuromorphic computing.[23]

The combination of NPC and PPC responses provides the possibility for the innovative applications of photodetectors in secure communications,[24] logic circuits,[25] and image processing.[26] However, switching between NPC and PPC in reported detectors primarily relies on wavelength control,[27–29] which requires wavelength conversion and cannot achieve synchronous temporal modulation. Besides, most devices exhibiting bipolar responses are limited to a certain group of materials with a particular structure such as 2D materials,[30,31] and their intrinsic properties restrict the long-term sustainable application in extreme environments, such as radiation detection, deep ultraviolet detection, and large-sized devices.[32–35] It is noteworthy that, in various architectures, heterojunctions can precisely control the band alignment according to the optical properties of different materials to achieve a customized spectral response.[36] Ga_2O_3 has a direct bandgap far exceeding that of materials such as GaN and SiC, with a high absorption coefficient and a transmittance of over 80% in the visible light region. It is resistant to high temperature, high pressure, and strong irradiation, demonstrating great potential in the field of deep ultraviolet detection.[37,38] On this basis, we found that Sb(V)-based oxides not only have good optical transparency but also exhibit a pronounced deep valence-band edge and a band structure matching that of Ga_2O_3.[39,40] By exploiting band-alignment characteristics and band engineering, integrating Sb_2O_5 and Ga_2O_3 into heterostructures can effectively enhance device detection performance, stability, and compatibility.

Therefore, in this study, we fabricated an a-Sb_2O_5/a-Ga_2O_3 heterostructure by magnetron sputtering and investigated its bipolar response characteristics of NPC and PPC with wavelength–voltage synergistic control. Due to carrier trapping at interface state defects, the heterojunction exhibits a maximal NPC response at 287 nm and 0 V bias, with a responsivity of 0.71 mA W^{-1}. Notably, as the voltage increases, the photocurrent polarity reverses at 0.5 V, showing wavelength-dependent polarity switching (short wavelength NPC response and long wavelength PPC response). When the voltage increases to 1 V, the detector exhibits the highest PPC responsivity of 1.05 mA W^{-1} at 303 nm, confirming the voltage-controlled photocurrent polarity switching. Furthermore, deep ultraviolet communication systems based on the detector can enhance optical communication confidentiality *via* bipolar coding and reduce bit error rates under extreme conditions through bipolar verification, thereby improving anti-interference capabilities. The wavelength–voltage synergistic control of photocurrent polarity switching exhibited by the a-Sb_2O_5/a-Ga_2O_3 heterojunction in the deep ultraviolet range enables the detector to have greater development potential for encryption and anti-interference communication, providing a foundation for developing novel optical communication devices.

2. Experimental

2.1. Fabrication of an a-Sb_2O_5/a-Ga_2O_3 heterojunction

Before sputtering, the ITO substrate was ultrasonically cleaned with acetone, anhydrous ethanol, and deionized water to eliminate contaminants from the substrate surface. After placing the sample in the chamber, the chamber was vacuumed to a pressure of 1×10^{-4} Pa, and the surface of the target was pre-sputtered before the formal deposition. The double-layer films of the a-Sb_2O_5/a-Ga_2O_3 heterostructure were fabricated by magnetron sputtering under high vacuum conditions throughout the process to ensure excellent interfacial contact. Additionally, since no temperature was applied during deposition, all films were deposited in an amorphous state.

Preparation of the a-Sb_2O_5 film. The a-Sb_2O_5 film was prepared on ITO substrates by radio-frequency (RF) magnetron sputtering. The solid Sb target (99.99%) was used as the sputtering target. The sputtering power was maintained at 60 W, with an Ar : O_2 gas mixture ratio of 3 : 1. The deposition pressure and rate were controlled at 1 Pa and 10 nm min^{-1}, respectively.

Preparation of the a-Ga_2O_3 film. The pulsed magnetron sputtering was employed to deposit the a-Ga_2O_3 film on the existing a-Sb_2O_5 layer. The liquid Ga (99.999%) was used as a sputtering target. The sputtering process was conducted at a voltage of 620 V, a current of 0.2 A, and a duty cycle of 20%, with an Ar : O_2 gas mixture ratio of 4.5 : 1. The deposition pressure and rate were maintained at 0.5 Pa and 70 nm min^{-1}, respectively.

2.2. Device fabrication

The detector electrodes were fabricated *via* RF magnetron sputtering. Ti/Au interdigital electrodes with a thickness of 40/60 nm, respectively, were sputtered on the surface of the a-Ga_2O_3 film using a customized mask. Ti (99.99%) was used as the sputtering target for the Ti electrode layer, which was deposited at 15 W for 20 minutes in a pure Ar atmosphere. Subsequently, the Au electrode layer was sputtered using an Au target (99.99%) at 10 W for 10 minutes. The chamber pressure was maintained at 0.5 Pa throughout the deposition process.

2.3. Characterization

Scanning electron microscopy (SEM) and atomic force microscopy (AFM) were employed to analyze the cross-section and surface of the films. Grazing incidence X-ray diffraction (GIXRD) and transmission electron microscopy (TEM) were used to investigate the structural characteristics of the films. X-ray photoelectron spectroscopy (XPS) was employed to determine the composition of the films. The transmission of UV light was measured using a UV-2550 UV-vis spectrometer. The energy band structure was characterized by ultraviolet photoelectron spectroscopy (UPS). The bipolar photoresponse properties (wavelength response, time-domain response, and *I–V* response) were evaluated using a Keithley 2636B UV photodetector test system. The underlying mechanism was further verified by photoluminescence (PL) spectroscopy.

3. Results and discussion

Fig. 1(a) exhibits the SEM cross-sectional image of the a-Sb_2O_5/a-Ga_2O_3 heterojunction clearly. The top layer is the a-Ga_2O_3 film with a thickness of about 700 nm, the middle layer is the a-Sb_2O_5 film of about 300 nm, and the bottom layer is the ITO transparent conductive electrode. It is seen that each layer of the heterojunction has a continuous and smooth surface, and the contact between the layers is tight. Fig. 1(b) and (d) show AFM images of the a-Sb_2O_5 and a-Ga_2O_3 films, respectively. From the images, it is noticed that both films exhibit closely packed granular structures, which are typical of magnetron sputtering morphology. Since no additional heating was applied during sputtering, the films are amorphous. Grazing incidence XRD (GIXRD) detected only weakened substrate peaks, with no characteristic peaks of Sb_2O_5 and Ga_2O_3 observed (Fig. S1 in the SI). Fig. 1(c) shows the XPS spectrum of the a-Sb_2O_5 film in which the Sb $3d_{5/2}$ peak is close to the O 1s peak, resulting in a coincident single peak. The ratio of Sb $3d_{5/2}$: Sb $3d_{3/2}$ is 1.45 after the peak separation, which is consistent with the peak area ratio proposed by Scofield. The peaks of Sb $3d_{5/2}$, Sb $3d_{3/2}$, and O 1s are located at 531.20 eV, 540.62 eV, and 531.44 eV, respectively. The half-peak widths of Sb $3d_{5/2}$ and Sb $3d_{3/2}$ are approximately 1.35 eV. The higher binding energy and narrow half-peak width further confirm that Sb is in the +5 oxidation state.[41] Fig. 1(e) and (f) exhibit the XPS spectra of Ga $2p_{3/2}$ and O 1s, respectively. The peak of Ga $2p_{3/2}$ is located at 1118.41 eV, and the strongest peak of O 1s is located at 531.05 eV, corresponding to lattice oxygen. The peak of the binding energy at 531.74 eV is related to the oxygen defect.[42] The atomic ratios of the a-Sb_2O_5 and a-Ga_2O_3 films obtained from XPS peak fitting closely match the theoretical stoichiometric ratios, and the elemental distribution in elemental mapping is uniform (Fig. S2 in the SI), indicating accurate film composition.

Fig. 2(a) shows the structural diagram of the detector. The Ti/Au electrode is used as the top electrode above the film, while ITO is employed as the bottom electrode, forming an a-Sb_2O_5/a-Ga_2O_3 vertical detector (the optical image of the device is shown in Fig. S3). The UV transmission spectra of the a-Sb_2O_5 and a-Ga_2O_3 films are shown in Fig. 2(b), both exhibiting sharp cut-off edges. According to Tauc plots, the evaluated band gap is 4.7 eV for a-Sb_2O_5 and 5.0 eV for a-Ga_2O_3. Fig. 2(c) shows the wavelength response of the detector in the range of 200–800 nm. It can be seen that the detector has good spectral

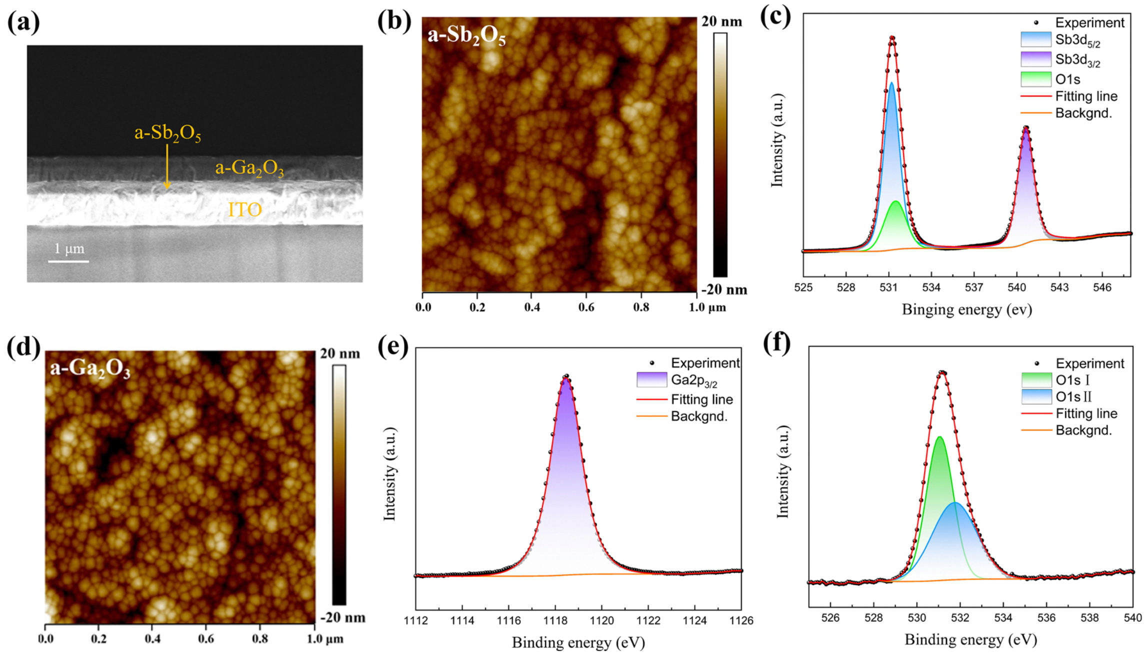

Fig. 1 Morphology and structural characterization of Sb_2O_5/a-Ga_2O_3 heterojunctions. (a) SEM image of the interface of the a-Sb_2O_5/a-Ga_2O_3 heterojunction. (b) AFM image of a-Sb_2O_5. (c) XPS image of a-Sb_2O_5. (d) AFM image of a-Ga_2O_3. (e) and (f) XPS images of a-Ga_2O_3.

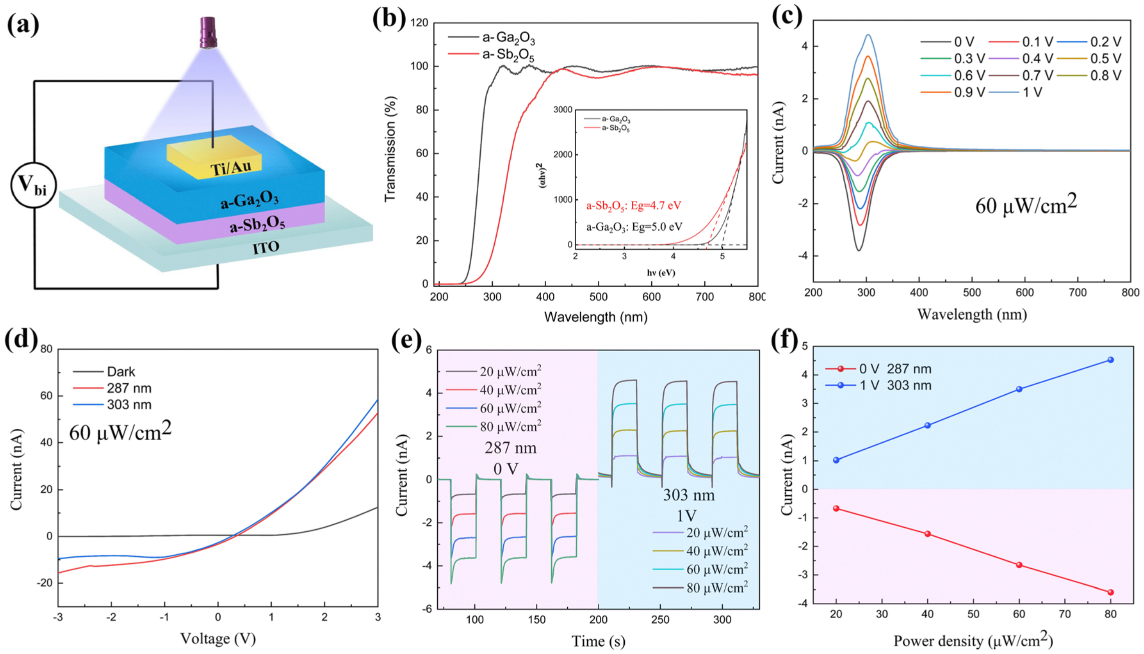

Fig. 2 Structure and photoelectric response measurement of the a-Sb_2O_5/a-Ga_2O_3 bipolar detector. (a) Schematic diagram of the a-Sb_2O_5/a-Ga_2O_3 detector. (b) UV transmission spectra and band gap diagrams of a-Sb_2O_5 and a-Ga_2O_3. (c) The wavelength response diagram of the detector under different voltages. (d) *I*–*V* images at 287 nm and 303 nm. (e) and (f) Power density-dependent time-domain photoresponse of the detector at different wavelengths.

selectivity and only responds in the UV range. When no voltage is applied, the detector exhibits a negative photoconductivity (NPC) response ($I_{\lambda287/\lambda400}$ = 422 at 0 V). As the applied voltage increases, the NPC response gradually weakens, and until 0.5 V, the current polarity reverses, displaying both the short-wavelength NPC response and the long-wavelength PPC response. When the voltage exceeds 0.5 V, the detector only exhibits a PPC response ($I_{\lambda303/\lambda400}$ = 45 at 1 V). The transition from NPC to PPC is accompanied by a decrease in the current suppression ratio. This is because, as the voltage increases, the number of carriers rises, leading to an increase in the current in the non-responsive state. In addition, it is worth noting that there is a shift between the NPC response peak and the PPC response peak of the detector. Short wavelengths (high photon energy) are more likely to generate an NPC response, while at long wavelengths (low photon energy), a PPC response is more easily generated.[43] This is consistent with the wavelength-dependent bidirectional photoresponse observed at 0.5 V bias. This is because the wavelength of the illumination also affects conductivity. At longer wavelengths, the photon energy decreases, reducing the light absorption capability of the a-Ga_2O_3 layer. As a result, interface state recombination caused by defects is reduced, making it easier to generate a PPC response. Fig. 2(d) shows the current–voltage (*I*–*V*) characteristics at different wavelengths, revealing the obvious rectification characteristics. At negative voltage, the negative photocurrent is larger under 287 nm; whereas at positive voltage, the positive photocurrent is larger under 303 nm. This is consistent with the wavelength dependence exhibited in the wavelength response. Fig. 2(e) displays the time-domain photoresponse at different power densities, where the photocurrent at 287 nm and 303 nm increases progressively and exhibits approximate linearity, as further quantified in Fig. 2(f). In addition, the device stability, reproducibility, and device-to-device uniformity are important components for measuring its application value. Stability tests were conducted on the performance of the device under 287 nm illumination at 0 V and 1 V voltages. According to the test results (Fig. S4 in the SI), after 40 rapid switching cycles, the response of the device did not experience significant attenuation, indicating good stability during operation. To assess the reproducibility and device-to-device uniformity, we collected test data on NPC (0 V bias) and PPC (1 V bias) responses measured by different devices under 287 nm illumination (Fig. S5 in the SI), and then evaluated the uniformity among devices using the relative standard deviation (RSD, the standard deviation expressed as a percentage of the mean). The calculated RSD was about 1%, indicating that the devices exhibit very good uniformity.

Fig. 3 shows the dual polarity photoresponse of the detector at wavelengths of 287 nm and 303 nm, respectively. Fig. 3(a) exhibits the variation in photocurrent polarity as a function of applied voltage under 287 nm illumination with a power density of 60 μW cm^{-2}. In the voltage range from 0 V to 0.5 V, the device exhibits an NPC response. This NPC response is attributed to the trapping of photo-generated carriers by defect states at the heterojunction interface.[44] As the external electric field strength increases, carriers are more likely to traverse the channel, reducing the number of trapped carriers. Due to the dominance of electric field-induced carrier drift and carriers released from traps, the observed NPC response decreases and transitions to a PPC response at 0.6 V. Because

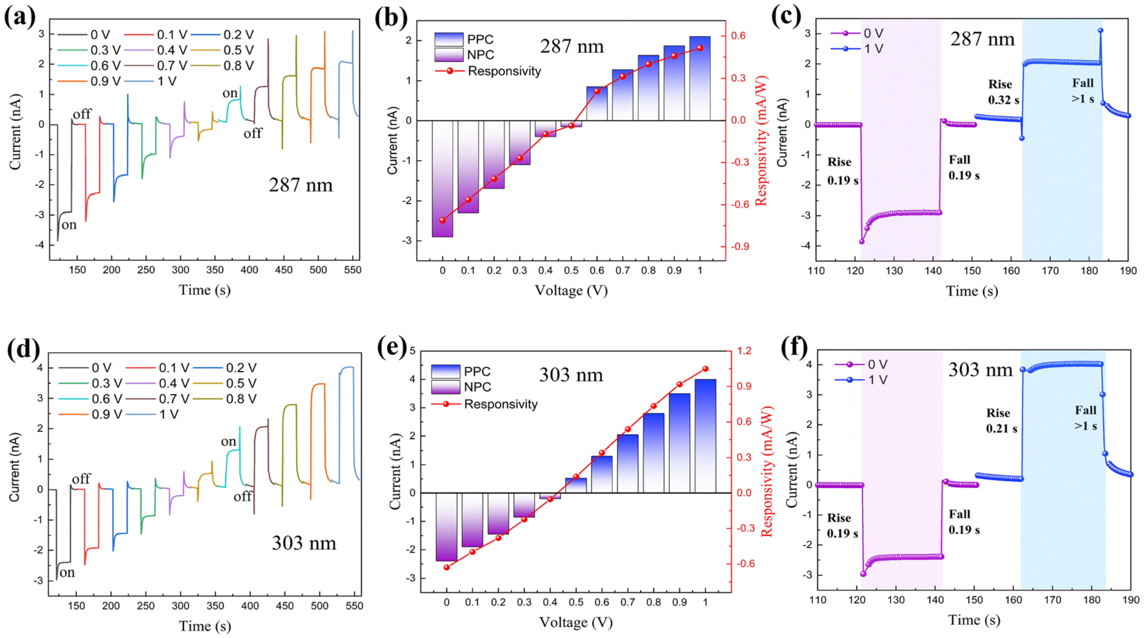

Fig. 3 Dual polarity photoresponse of the detector at 287 nm and 303 nm. (a) and (b) Voltage-dependent dual polarity photoresponse of the detector at 287 nm. (c) The rise and fall times of photocurrent at 287 nm. (d) and (e) Voltage-dependent dual polarity photoresponse of the detector at 303 nm. (f) The rise and fall times of photocurrent at 303 nm.

of the different wavelengths for NPC and PPC responses, the responsivity increase of PPC (0.52 mA W^{-1} at 1 V) is notably lower than that of NPC (0.71 mA W^{-1} at 0 V) at 287 nm (Fig. 3(b)). Fig. 3(d) exhibits the photocurrent polarity shift with increasing voltage under 303 nm illumination. Due to the decrease in photon energy, the optical absorption of a-Ga_2O_3 weakens, and the interface state recombination caused by defects is reduced, making it easier to generate a PPC response. Compared to 287 nm, under 303 nm illumination, the NPC response weakens (0.63 mA W^{-1} at 0 V), the PPC response is significantly enhanced (1.05 mA W^{-1} at 1 V), and the PPC response emerges at 0.5 V, with a reduced transition voltage (Fig. 3(e)). This switching further confirms that the negative response originates from defect states at the interface. Notably, NPC responses at both wavelengths exhibit fast response characteristics, whereas the PPC response shows prolonged response times due to increased carrier concentration, indicating a persistent photoconductivity effect (Fig. 3(c) and (f)). Fig. 3(a) and (d) reveal that both NPC and PPC responses have a convex non-equilibrium current, which is also caused by the carrier recombination from internal defect states within the heterojunction. The presence of trap energy levels influences carrier generation and recombination; carrier capture at these levels reduces carrier concentration in the valence and conduction bands, producing the observed non-equilibrium current.[45] At 303 nm, as the PPC response and the number of carriers increases, the impact of carrier recombination caused by internal trap states on the photocurrent gradually decreases, and the non-equilibrium current gradually disappears. In addition, because traps formed by interface states hinder efficient carrier transport in the device, the bipolar response of this detector is lower than the photocurrent of traditional deep ultraviolet detectors. However, compared with other devices that exhibit bipolar responses (Table 1), the a-Sb_2O_5/a-Ga_2O_3 photodetector

Table 1 Comparison of NPC and PPC responses of the studied film with other materials

Materials	Wavelength (nm)	Responsivity	Voltage (V)	NPC–PPC switching	Ref.
ZnO/SnS	365	155 μA W^{-1}	0	λ	29
Nb_3Cl_8	400	156.82 mA W^{-1}	3	λ	46
Ga_2O_3/Cu_2O	365	0.57 mA W^{-1}	0	λ	47
$MoTe_2$/SnS_2	465	5000 A W^{-1}	1	λ	30
Graphene/InSe/h-BN	405	1.1×10^4 A W^{-1}	0	P	48
Bi_2Se_3/Sb_2Se_3	1064	4 mA W^{-1}	0	V	44
	532	15 mA W^{-1}	0		
InAs NWs	500	3×10^4 A W^{-1}	0.2	λ	49
$Cs_3Bi_2Cl_9$	White light	17 mA W^{-1}	5	λ	50
ZnO/Sb_2Se_3	405	3.7 μA W^{-1}	0	λ	22
a-Sb_2O_5/a-Ga_2O_3	287	0.71 mA W^{-1}	0	λ and V	This work
	303	1.05 mA W^{-1}	1		

achieves bipolar modulation at shorter wavelengths, and its responsivity in the ultraviolet range exceeds that of many previously reported bipolar response detectors. Furthermore, due to the lower dark current in the NPC response compared to the PPC response, the NPC response has higher detectivity at low voltage (Fig. S6 in the SI), which is more favorable for the fabrication of low-power devices.

To illustrate the dynamics of carriers, the work function of the material was measured using ultraviolet photoelectron spectroscopy (UPS), and the energy band structure diagram of the a-Sb_2O_5/a-Ga_2O_3 heterojunction was shown (Fig. 4(a) and (b)). From the UPS measurements, it is found that the work function of a-Sb_2O_5 is 3.61 eV, and that of a-Ga_2O_3 is 3.09 eV. The difference in work functions leads to band bending at the interface of the a-Sb_2O_5/a-Ga_2O_3 heterojunction, forming a type-II band alignment under equilibrium conditions. Both the a-Sb_2O_5 and a-Ga_2O_3 layers absorb ultraviolet light to generate electron–hole pairs. Under ultraviolet light illumination, interface state defects cause the recombination of photogenerated electrons in Ga_2O_3 and photogenerated holes in Sb_2O_5. The remaining photoholes in a-Ga_2O_3 and the remaining photoelectrons in a-Sb_2O_5 cannot migrate to the other side to produce an effective drift current because of the potential barrier. Consequently, at 0 V bias, the recombination current inside the heterojunction dominates, resulting in a negative photoconductivity (NPC). To demonstrate the effect of interface state defects on carrier recombination, we tested the photoluminescence (PL) spectra (Fig. S7(a) in the SI) of the samples and found that the emission intensity of the heterojunction was significantly reduced compared to the a-Ga_2O_3 film. This pronounced PL quenching suggests that excitons dissociate into electrons and holes, which are then captured and recombine as charge carriers. In addition, we also tested time-resolved photoluminescence (TRPL) spectra (Fig. S7(b) in the SI). According to the experimental data, the carrier lifetime in the heterojunction decreases compared to the a-Ga_2O_3 film (from 4.3536 ns to 3.9866 ns), indicating the presence of trap-assisted carrier recombination. This further confirms the role of interface state defects in capturing carriers and supporting the mechanism for the NPC response. As the applied voltage increases, the external field more strongly influences the carriers and generates a weak drift current; the competition between the drift current and the recombination current weakens the NPC response. Due to the applied voltage, the height of the barrier decreases. When the external field exceeds the switching voltage, carriers overcome the barrier and form a large drift current along the field direction, causing a reversal of the current polarity and producing a positive photocurrent. To further demonstrate the effect of interface state defects on switching voltage, we adjusted the oxygen pressure (Fig. S8 in the SI) and annealing (Fig. S9 in the SI) temperature during the preparation process, and tested the bipolar response of the device under 287 nm light illumination. By adjusting the oxygen pressure during sputtering of the Sb_2O_5 layer, it was found that the switching voltage of the detector increases with the decrease of oxygen pressure (gradually increasing from 0.4 V to 0.7 V). In addition, the rapid thermal annealing (RTA) of the devices in an oxygen atmosphere at different temperatures showed that when the temperature reached 300 °C, the NPC response decreased to one-third of its original value, and the switching voltage fell from 0.6 V to 0.4 V. When the temperature was raised to 400 °C, the device completely converted to a PPC response. This further confirms that the bipolar switching is caused by interface state defects.

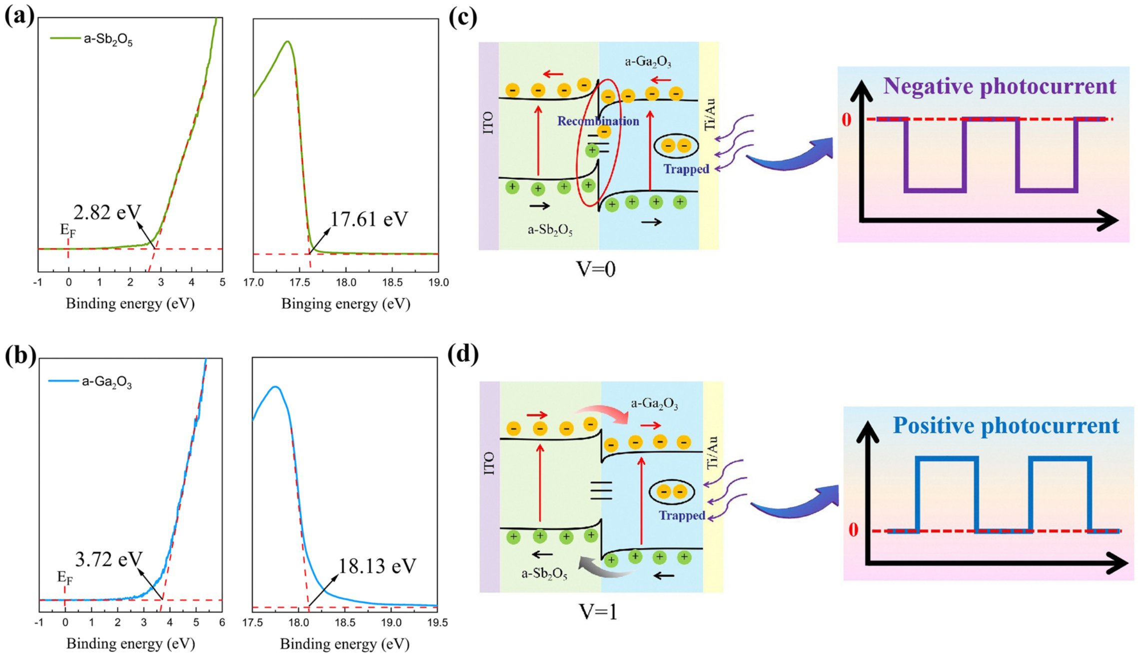

Fig. 4 Schematic diagram of the energy bands and interfacial carrier transfer mechanism of the a-Sb_2O_5/a-Ga_2O_3 bipolar detector. (a) UPS spectrum of a-Sb_2O_5 (b) UPS spectrum of a-Ga_2O_3. (c) NPC response mechanism of the detector under 0 V. (d) PPC response mechanism of the detector under 1 V.

In traditional optical communication, information is converted into ASCII code and transmitted *via* optical signals, where the on and off states of light represent the binary signals ''1'' and ''0'', respectively.[51] For traditional photodetectors, only single-channel information transmission is possible, and unable to realize the common transmission of information and key. This results in the sender and receiver only being able to transmit information using pre-agreed keys, making real-time key changes impossible and easily causing information leakage. The bipolar response detector can exhibit photoresponses of opposite polarity under different conditions, and it can use the NPC and PPC responses to transmit encrypted information and keys (Fig. 5). Specifically, in the encrypted mode, wavelength modulation is primary and the voltage is set at 0.5 V; ultraviolet light at 287 nm (NPC) and 303 nm (PPC) are used as the communication sources to illuminate the devices, respectively (Fig. S10(a) in the SI). The PPC response at 303 nm carries the encrypted information, while the NPC response at 287 nm serves as the real-time key. Only when the real-time key and the encrypted information are obtained simultaneously can the information be decoded completely and accurately. As shown in Fig. 6(a), the transmission information is first converted into binary using the ASCII code. Taking ''NEWS'' as an example, its corresponding ASCII codes are ''01001110'', ''01000101'', ''01010111'', and ''01010011'', respectively. The irregular keys transmitted in real-time through the NPC channel are used to perform encryption operations on the original information, and then the encrypted information is synchronously transmitted through the PPC channel. When the receiver obtains all the information, the system then performs decryption operations using the real-time key to retrieve the original information. This means that, compared to traditional optical communication systems, the bipolar response system can achieve real-time changes in encryption algorithms, enhancing the randomness of the keys and significantly improving the security of the communication system.

Additionally, in some extreme environments, external factors can interfere with communication systems, causing errors in the transmission of ''0'' and ''1'' signals, which leads to information being unrecognizable or even misrecognized.[52] Therefore, we have developed an anti-interference mode for bipolar detectors to improve the accuracy and integrity of information transmission (Fig. 6(b)). In this mode, the voltage modulation is primary, with a fixed wavelength of 287 nm and the two device voltages set to 0 V (NPC) and 1 V (PPC), respectively (Fig. S10(b) in the SI). To achieve error monitoring, we added an additional check bit after encoding: when the number of ''1'' in the transmitted information is even, the check bit is encoded as ''0'', known as an even check; otherwise, it is an odd check, with the check bit encoded as ''1''. However, parity checks can only detect an odd number of bit errors; when an even number of bit errors occur, the system cannot accurately identify them, and the parity check will still pass successfully. To solve this problem, we further implemented error monitoring by adding redundant codes to the channel coding. The original ''0'' code is replaced by the ''00'' code, and the original ''1'' code is replaced by the ''11'' code. These redundant code symbols do not contain communication information but are transmitted simultaneously with the information code symbols. When the error code appears in different signals, the code length at the corresponding position changes significantly, allowing the system to accurately identify the error location. When two adjacent codes in the same signal simultaneously change from ''00'' to ''11'' (the recognized signal changes from ''0'' to ''1''), the code length does not change significantly, but the parity of the code changes, and the parity check fails. The addition of redundant codes enables the system to detect most even-number code errors, greatly compensating for the inability of parity checks. Moreover, the bidirectional photoresponse system can synchronously transmit information through bipolar channels with opposite current polarity, and the characteristic of bipolar current makes

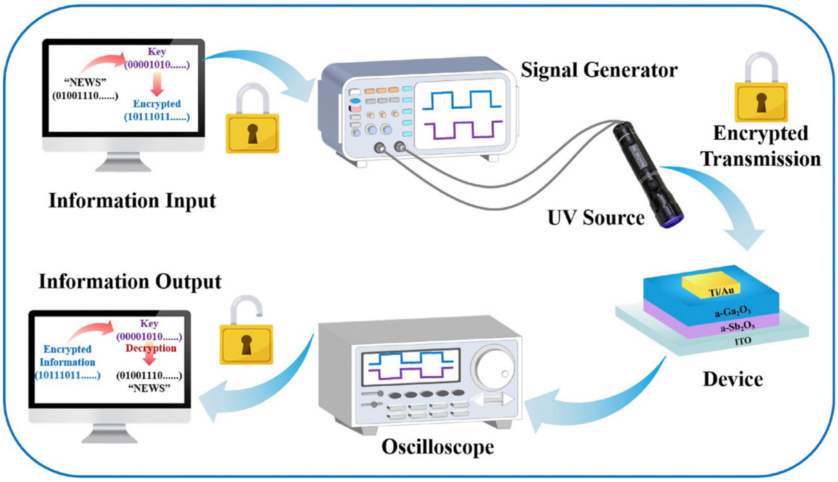

Fig. 5 Schematic diagram of an optical communication system combining the bipolar response of NPC and PPC. The NPC response serves as the key channel to transmit the real-time key, while the PPC response serves as the information channel to transmit the encrypted information encrypted by the real-time key.

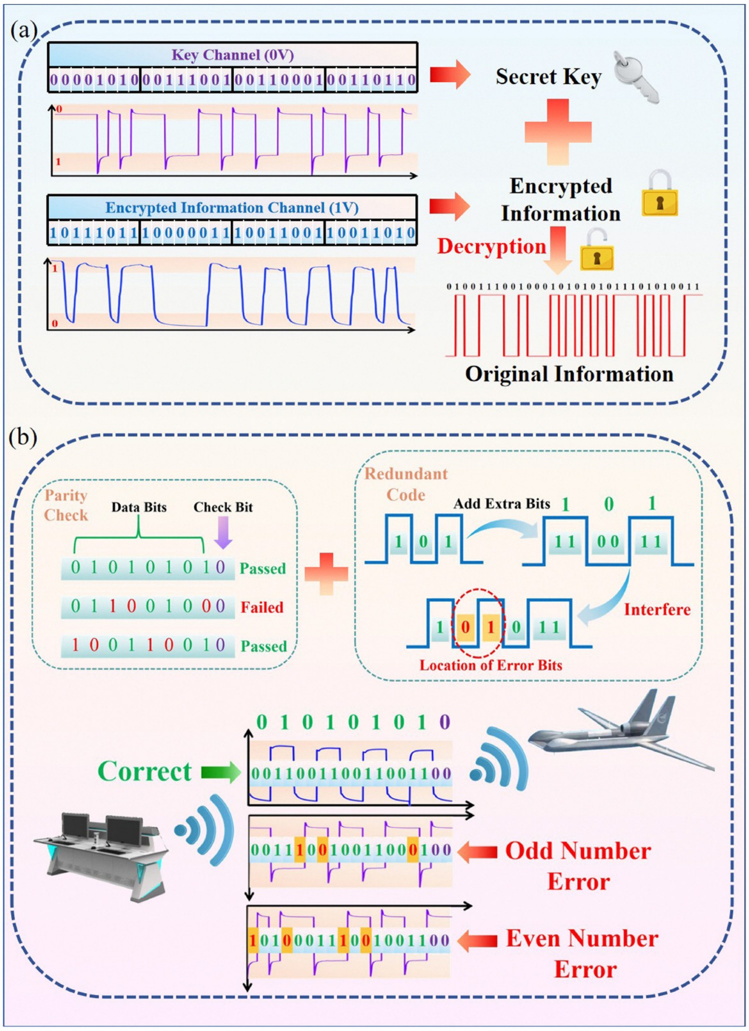

Fig. 6 Two communication modes of a bipolar optical communication system. (a) Real-time encryption mode in an optical communication system. (b) Anti-interference and error correction mode in an optical communication system.

the situation where both channels are simultaneously interfered with relatively few. Therefore, when an error is detected in one channel, the parity check and redundant code can accurately identify the error and determine its position. After the error is determined, the error correction can be performed through another unaffected information channel. If the decoded information from both channels is consistent, the transmission is considered to be correct. This system not only accurately identifies errors and determines the positions of the error code, but also corrects errors, reducing the bit error rate and improving the anti-interference ability of the communication system in a complex environment.

4. Conclusions

In summary, an a-Sb_2O_5/a-Ga_2O_3 deep-UV photodetector was fabricated using magnetron sputtering technology. The detector exhibits a unique bidirectional photoresponse that is controlled synergistically by wavelength and voltage, and its potential application in real-time encryption and anti-interference communication is demonstrated. Analysis of the wavelength response, time-domain response, and *I–V* response revealed that the detector exhibits excellent spectral selectivity, only responding to the UV light. At 0 V bias, interface trapping effects induce an NPC response with a responsivity of 0.71 mA W^{-1}; as the applied voltage increases, the NPC response gradually decreases under the influence of the applied electric field. At a bias of 0.5 V, both the short-wavelength (high photon energy) NPC response and the long-wavelength (low photon energy) PPC response are observed simultaneously. When the voltage exceeds 0.5 V, the detector exhibits only the PPC response under the applied electric field. Furthermore, compared to illumination at 287 nm, the NPC response weakens at 303 nm (0.63 mA W^{-1} at 0 V), while the PPC response is significantly enhanced (1.05 mA W^{-1} at 1 V). The deep-ultraviolet communication system constructed based on the wavelength–voltage synergistically controlled bipolar response not only achieves synchronous transmission of bipolar coding and real-time key updates, enhancing the security of the optical communication system; it also utilizes the redundancy of bipolar channels for error detection and correction, reducing the bit error rate of the detector in extreme environments and improving its anti-interference capability. The unique wavelength–voltage controlled photocurrent polarity switching of the a-Sb_2O_5/a-Ga_2O_3 detector in the deep-UV range exhibits excellent potential for encrypted and anti-interference communication, and provides a novel approach to developing innovative multi-functional optoelectronic devices.

Author contributions

Cheng Wu: writing – original draft. Peiwen Lv: writing – review & editing, and supervision. Zhaojie Zhu: supervision. Yizhi Huang: resources. Chaoyang Tu: supervision. Chenlong Chen: supervision. G. Lakshminarayana: formal analysis. Yan Wang: writing – review & editing, and funding acquisition.

Conflicts of interest

The authors declare no competing financial interest.

Data availability

The data supporting this article have been included as part of the supplementary information (SI). Supplementary information is available. See DOI: **https://doi.org/10.1039/d5mh01415h**.

Acknowledgements

This work was supported by the Advanced Materials-National Science and Technology Major Project 2030, the 06 Major Project of Ministry of Industry and Information Technology of China (2024ZD0606000), the National Key Research and Development Program of China (Grant No. 2022YFB3605700), the Science and Technology Plan Leading Project of Fujian Province (Grant No. 2024H0033 and 2022H0043), the National Nature Science Foundation of China (Grant No. 51832007 and 51872286), the NSFC-Joint Funds for Regional Innovation and Development (Grant No. U21A20508), the Fujian Science & Technology Innovation Laboratory for Optoelectronic Information of China (Grant No. 2021ZR204 and 2020zz108), and the 14th Five-year Plan Project of FJIRSM (Grant No. E255KL0101).

References

1 Z. Q. Li, T. T. Yan and X. S. Fang, *Nat. Rev. Mater.*, 2023, **8**, 587–603.

2 X. L. Deng, Z. Q. Li, F. Cao, E. L. Hong and X. S. Fang, *Adv. Funct. Mater.*, 2023, **33**, 2213334.

3 Z. J. Lan, Y. S. Lau, L. F. Cai, J. Y. Han, C. W. Suen and F. R. Zhu, *Laser Photonics Rev.*, 2022, **16**, 2100602.

4 Q. C. Zhang, Q. H. Tan, J. Ding, X. B. Feng, P. Z. Yang, Y. K. Liu and Q. J. Wang, *Nano Res.*, 2025, **18**, 94906990.

5 H. B. Li, C. H. Li, M. Peng, K. H. Li, C. Chen, Y. X. Chen, Z. H. Zheng, Z. H. Su, G. X. Liang and S. Chen, *Adv. Funct. Mater.*, 2025, 2425690, in press.

6 Y. J. Liu, Y. X. Gao, J. Y. Zhi, R. Q. Huang, W. J. Li, X. Y. Huang, G. H. Yan, Z. Ji and W. J. Mai, *Nano Res.*, 2021, **15**, 1094–1101.

7 J. Y. Wang, C. C. Ling, X. Xue, H. G. Ji, C. Rong, Q. Z. Xue, P. H. Zhou, C. K. Wang, H. P. Lu and W. P. Liu, *Small*, 2024, **20**, 2310107.

8 H. Y. Guan, G. J. Mao, T. Y. Zhong, T. M. Zhao, S. Liang, L. L. Xing and X. Y. Xue, *J. Alloys Compd.*, 2021, **867**, 159073.

9 V. Laxmi, Y. D. Tu, D. Tyagi, P. K. Nayak, Y. B. Tian and W. J. Zhang, *Nanoscale*, 2025, **17**, 11246–11274.

10 H. R. Liang, Y. H. Ma, H. X. Yi and J. D. Yao, *Materials*, 2023, **16**, 7372.

11 Y. Y. Yu, M. Peng, F. Zhong, Z. Wang, X. Ge, H. Chen, J. X. Guo, Y. Wang, Y. Chen, T. F. Xu, T. G. Zhao, T. He, K. Zhang, F. Wu, C. Q. Chen, J. N. Dai and W. D. Hu, *Mater. Horiz.*, 2023, **10**, 2579–2586.

12 C. Xie and F. Yan, *Small*, 2017, **13**, 1701822.

13 S. Suman, U. Pandey, N. Pal, P. Swaminathan and B. N. Pal, *ACS Photonics*, 2024, **11**, 93–101.

14 J. R. Nasr, N. Simonson, A. Oberoi, M. W. Horn, J. A. Robinson and S. Das, *ACS Nano*, 2020, **14**, 15440–15449.

15 X. H. Hou, C. Li, C. Chen, S. Y. Bai, Y. Liu, Z. X. Peng, X. L. Zhao, X. Z. Zhou, G. W. Xu, N. Gao and S. B. Long, *Adv. Mater.*, 2025, 2506179, in press.

16 S. H. Aleithan and W. Ahmad, *Mater. Today Energy*, 2025, **51**, 101906.

17 J. N. Wang, G. Y. Tao, Z. M. Zhang, Y. H. Li, S. M. Xiao, C. R. Huang, Q. H. Song, H. K. Tsang and K. Xu, *Laser Photonics Rev.*, 2025, **19**, 2402072.

18 P. S. Li, Z. X. Sa, Z. Q. Zang, G. C. Wang, M. X. Wang, L. Liao, F. Chen and Z. X. Yang, *Mater. Horiz.*, 2025, **12**, 5357.

19 E. Baek, T. Rim, J. Schutt, C. K. Baek, K. Kim, L. Baraban and G. Cuniberti, *Nano Lett.*, 2017, **17**, 6727–6734.

20 D. Xue, W. J. Gong, C. Yan, Y. Y. Zhang, J. Lu, Y. Yin, J. D. Zhang, Z. Wang, L. Z. Huang and L. F. Chi, *Adv. Funct. Mater.*, 2024, **34**, 2402884.

21 H. J. Xu, Y. X. Weng, K. Chen, C. Wu, H. Z. Hu and D. Y. Guo, *Adv. Opt. Mater.*, 2024, **13**, 2402238.

22 B. S. Ouyang, H. Q. Zhao, Z. L. Wang and Y. Yang, *Nano Energy*, 2020, **68**, 104312.

23 H. Y. Tang, T. Anwar, M. S. Jang and G. Tagliabue, *Adv. Sci.*, 2024, **11**, 2309876.

24 S. Fang, L. A. Li, W. Y. Wang, W. Chen, D. H. Wang, Y. Kang, X. Liu, H. F. Jia, Y. M. Luo, H. B. Yu, M. H. Memon, W. Hu, B. S. Ooi, J. H. He and H. D. Sun, *Adv. Mater.*, 2023, **35**, 2300911.

25 W. Chen, D. H. Wang, W. Y. Wang, Y. Kang, X. Liu, S. Fang, L. A. Li, Y. M. Luo, K. Liang, Y. Y. Liu, D. Y. Luo, M. H. Memon, H. B. Yu, W. G. Gu, Z. H. Liu, W. Hu and H. D. Sun, *Adv. Mater.*, 2024, **36**, 2307779.

26 P. S. Li, H. L. Song, Z. X. Sa, F. J. Liu, M. X. Wang, G. C. Wang, J. C. Wan, Z. Q. Zang, J. Jiang and Z. X. Yang, *Mater. Horiz.*, 2024, **11**, 4979.

27 X. Z. Wang, D. Pan, M. Sun, F. J. Lyu, J. H. Zhao and Q. Chen, *ACS Appl. Mater. Interfaces*, 2021, **13**, 26187–26195.

28 H. Jawa, A. Varghese, S. Ghosh, S. Sahoo, Y. F. Yin, N. V. Medhekar and S. Lodha, *Adv. Funct. Mater.*, 2022, **32**, 2112696.

29 B. S. Ouyang, K. W. Zhang and Y. Yang, *iScience*, 2018, **1**, 16–23.

30 Y. Jeong, T. Kim, H. Cho, J. Ahn, S. Hong, D. K. Hwang and S. Im, *Adv. Mater.*, 2023, **35**, 2304599.

31 J. Y. Wu, Y. T. Chun, S. P. Li, T. Zhang, J. Z. Wang, P. K. Shrestha and D. P. Chu, *Adv. Mater.*, 2018, **30**, 1705880.

32 L. Chen, J. J. Tai, D. Y. Wang, S. Wang, H. W. Liang and H. Yin, *Appl. Phys. Lett.*, 2024, **124**, 042102.

33 J. Ahn, E. Yeon and D. K. Hwang, *Adv. Opt. Mater.*, 2025, **13**, 2403412.

34 S. Ghosh, A. Varghese, H. Jawa, Y. F. Yin, N. V. Medhekar and S. Lodha, *ACS Nano*, 2022, **16**, 4578–4587.

35 Y. Wang, Y. H. Li, C. Li, C. Wang, Q. Zhou, L. S. Liang, Z. L. Zhang, C. M. Liu, W. Yu, X. T. Yu and P. Gao, *Small*, 2024, **20**, 2402531.

36 S. He, P. Feng, Y. Du, Y. Ma, C. Dang, A. Shan, L. Zhao, T. Wei, M. Li and L. Gao, *Adv. Opt. Mater.*, 2024, **12**, 2302399.

37 K. Peng, D. F. Xue, N. Y. Li, W. Lin, C. L. Chen and P. W. Lv, *ACS Appl. Mater. Interfaces*, 2025, **17**, 43199–43207.

38 J. Zhang, F. J. Liu, D. Liu, Y. X. Yin, M. X. Wang, Z. X. Sa, L. Sun, X. X. Zheng, X. M. Zhuang, Z. T. Lv, W. X. Mu, Z. T. Jia, Y. Tan, F. Chen and Z. X. Yang, *Mater. Today Phys.*, 2023, **31**, 100997.

39 R. Claes and D. O. Scanlon, *Phys. Status Solidi RRL*, 2025, 2400399.

40 K. Li, J. Willis, S. R. Kavanagh and D. O. Scanlon, *Chem. Mater.*, 2024, **36**, 2907–2916.

41 F. Garbassi, *Surf. Interface Anal.*, 1980, **2**, 165–169.

42 J. Huang, Y. Hu, T. Y. Zou, K. Tang, Z. L. Zhang, Y. C. Ma, B. Li, L. J. Wang and Y. C. Lu, *Surf. Coat. Technol.*, 2019, **366**, 70–74.

43 Y. X. Han, M. Q. Fu, Z. Q. Tang, X. Zheng, X. H. Ji, X. Y. Wang, W. J. Lin, T. Yang and Q. Chen, *ACS Appl. Mater. Interfaces*, 2017, **9**, 2867–2874.

44 K. Kumar, P. Sharma, S. Verma, S. K. Saini, N. K. Kumar Tailor, S. Husale, R. K. Singh, S. Satapathi, V. G. Achanta and M. Kumar, *Adv. Funct. Mater.*, 2024, **34**, 2405364.

45 Q. Q. He, G. Y. Chen, Y. K. Wang, X. Y. Liu, D. T. Xu, X. X. Xu, Y. Liu, J. C. Bao and X. Wang, *Small*, 2021, **17**, 2101403.

46 B. Lee, X. Zhang, J. Kang, B. J. Jeong, S. Cho, K. H. Choi, J. Jeon, S. H. Lee, D. Kim, Y. H. Kim, J. H. Kim, H. K. Yu and J. Y. Choi, *Nanoscale*, 2024, **16**, 20312–20318.

47 C. R. He, D. Y. Guo, K. Chen, S. L. Wang, J. Q. Shen, N. Zhao, A. P. Liu, Y. Y. Zheng, P. G. Li, Z. P. Wu, C. R. Li, F. M. Wu and W. H. Tang, *ACS Appl. Nano Mater.*, 2019, **2**, 4095–4103.

48 Z. T. Gao, R. Q. Jiang, M. H. Deng, C. Zhao, Z. Hong, L. Y. Shang, Y. W. Li, L. Q. Zhu, J. Z. Zhang, J. Zhang and Z. G. Hu, *Adv. Mater.*, 2024, **36**, 2401585.

49 Y. M. Yang, X. Y. Peng, H. S. Kim, T. Kim, S. Jeon, H. K. Kang, W. Choi, J. D. Song, Y. J. Doh and D. Yu, *Nano Lett.*, 2015, **15**, 5875–5882.

50 N. K. Tailor, P. Maity, M. I. Saidaminov, N. Pradhan and S. Satapathi, *J. Phys. Chem. Lett.*, 2021, **12**, 2286–2292.

51 T. Zhang, G. D. Wu, J. Y. Wang, R. X. Du, H. W. Lin, Y. Ren and L. Tao, *ACS Appl. Mater. Interfaces*, 2024, **16**, 33819–33828.

52 T. Yoshikawa, M. Ishimaru, T. Iwata, F. Mori and K. Kobayashi, *J. Electron. Test.*, 2022, **37**, 675–684.